



---

1 **Influence of bank slope on sinuosity-driven hyporheic exchange flow and**  
2 **residence time distribution during a dynamic flood event**

3

4 **Manuscript submitted to Hydrology and Earth System Sciences**

5

6 Yiming Li<sup>1,2</sup>, Uwe Schneidewind<sup>2</sup>, Zhang Wen<sup>1\*</sup>, Stefan Krause<sup>2</sup>, Hui Liu<sup>1</sup>

7

8 <sup>1</sup>Hubei Key Laboratory of Yangtze River Catchment Environmental Aquatic Science,  
9 School of Environmental Studies, China University of Geosciences, People's  
10 Republic of China

11 <sup>2</sup>School of Geography, Earth and Environmental Sciences, University of Birmingham,  
12 UK

13

14 **\*Correspondence:** Zhang Wen ([wenz@cug.edu.cn](mailto:wenz@cug.edu.cn))



15 **Abstract.** This study uses a reduced-order two-dimensional (2-D) horizontal model to  
16 investigate the influence of riverbank slope on the bank storage and sinuosity-driven  
17 hyporheic exchange flux (HEF) along sloping alluvial riverbanks during a transient  
18 flood event. The Deformed Geometry Method (DGM) is applied to quantify the  
19 displacement of the sediment-water interface (SWI) along the sloping riverbank  
20 during river stage fluctuation. This new model approach serves as the initial step to  
21 consider complicated floodplain morphologies in physics-based models for better  
22 predictions of HEF. Several controlling factors, including sinuosity, alluvial valley  
23 slope, and river flow advective forcing and duration of flow are incorporated in the  
24 model to investigate the effects of bank slope in aquifers of variable hydraulic  
25 transmissivity. Compared to simulations of a vertical riverbank, sloping riverbanks  
26 were found to increase the HEF. For sloping riverbanks, the hyporheic zone (HZ)  
27 encompass larger area and penetrated deeper into the alluvial aquifer, especially  
28 in aquifers with smaller transmissivity (i.e., larger aquifer hydraulic conductivity or  
29 smaller specific yield). Furthermore, consideration of sloping banks as compared to a  
30 vertical river bank can lead to both underestimation or overestimation of the pore  
31 water residence time. The impact of bank slope on residence time was more  
32 pronounced during a flood event for high transmissivity aquifer conditions, while it  
33 had a long-lasting influence after the flood event in lower transmissivity aquifers.  
34 Consequently, this decreases the residence time of HEF relative to the base flow  
35 condition. These findings highlight the need for (re)consideration of the importance of  
36 more complex riverbank morphology as control of hyporheic exchange in alluvial  
37 aquifers. The results have potential implications for river management and restoration  
38 and the management of river and groundwater pollution.

39  
40 **Key words:** hyporheic exchange, sloping riverbank, transient river stage, peak flow  
41 event, residence time distribution

42



### Nomenclature

$\Delta L$	Nodal spacing [m]
$\nabla$	Laplace operator
$\alpha_L$	Longitudinal dispersivity [L]
$\alpha_T$	Transverse dispersivity [L]
<b>D</b>	Dispersion-diffusion tensor [ $L^2T^{-1}$ ]
$D_L$	Water diffusivity [ $L^2T^{-1}$ ]
$J_x$	Base groundwater gradient [-]
$K$	Hydraulic conductivity [ $LT^{-1}$ ]
$n$	Scaling number [-]
$n_0$	Intensity of flood event [-]
$n_d$	Skewness of flood event [-]
$S_y$	Specific yield [-]
$t_d$	Duration of flood event [T]
$t_p$	Time to peak river stage [T]
$\alpha$	Amplitude of the river boundary [L]
$\Gamma_d$	Dimensionless aquifer transmissivity [-]
$\delta$	Bank slope angle [ $^\circ$ ]
$\delta_{ij}$	Kronecker delta function [-]
$\epsilon$	Tortuosity [-]
$\eta$	Degree of flood event asymmetry [ $T^{-1}$ ]
$\theta$	Effective porosity [-]
$\lambda$	River boundary wave length [L]
$\sigma$	River boundary sinuosity [-]
$\tau$	Residence time [T]
$\omega$	Flood event frequency [ $T^{-1}$ ]
$h(\mathbf{x}, t)$	Transient groundwater head [L]
$\Delta h^*$	Dimensionless parameter of ambient groundwater flow [-]



$A^{**}(t)$	Dimensionless variation of HZ area relative to base flow conditions [-]
$C(\mathbf{x}, t)$	Solute concentrations in the aquifer [ML <sup>-3</sup> ]
$C_0(\mathbf{x})$	Solute concentrations in initial condition [ML <sup>-3</sup> ]
$C_s(\mathbf{x}, t)$	Solute concentrations in the river [ML <sup>-3</sup> ]
$d^{**}(t)$	Dimensionless variation of HZ penetration distance relative to base flow conditions [-]
$H(\mathbf{x}, t)$	Thickness of the saturated aquifer [L]
$H_0(\mathbf{x})$	Initial river stage [L]
$H_p$	Peak river stage during the flood event [L]
$H_r(t)$	River stage at the downstream end [L]
$h_r(x, t)$	Transient river stage [L]
$M(t)$	Displacement of the sediment-water interface [L]
$P_e$	Péclet number [-]
$\mathbf{q}$	Specific discharge or Darcy flux [LT <sup>-1</sup> ]
$\mathbf{Q}$	Aquifer-integrated discharge [L <sup>2</sup> T <sup>-1</sup> ]
$Q_{in, HZ}^*(t)$	Dimensionless net flux along the river boundary [-]
$Q_{in, HZ}^*(t)$	Dimensionless exchange flux from the aquifer to the river [-]
$Q_{out, HZ}^*(t)$	Dimensionless exchange flux from the river to the aquifer [-]
$Y(x, t)$	Location of the sediment-water interface boundary [L]
$z_b(\mathbf{x})$	Elevation of the underlying impermeable layer [L]
$\Gamma_d$	Dimensionless parameter of aquifer transmissivity [-]
$\mu(\mathbf{x}, 0)$	Mean (first order of) residence time distribution [T]
$\mu_{out}^*(x, t)$	Flux-weighted ratio of mean RT to mean RT under baseflow conditions [-]
$\mu_n(\mathbf{x}, t)$	$n$ -th moment of residence time distribution [T <sup><math>n</math></sup> ]
$\mu_r^*(\mathbf{x}, t)$	Residence time distribution ratio between slope and vertical river bank model [-]
$\mu_{\tau 0-\max}$	Maximum RT in the domain [T]



$\mu_{\tau,s}(\mathbf{x}, t)$	Residence time distribution of slope river bank model [T]
$\mu_{\tau,v}(\mathbf{x}, 0)$	Residence time distribution of vertical river bank model [T]
$\rho(\mathbf{x}, t, \tau)$	Residence time distribution [T]

#### Abbreviations

HZ	Hyporheic zone
HEF	Hyporheic exchange flux
DGM	Deformed Geometry Method
SWI	Sediment-water interface
RTD	Residence time distribution
RT	Residence time
ALE	Arbitrary Lagrangian–Eulerian
2-D	Two-dimensional

43

44



---

## 45 1. Introduction

46 The hyporheic zone (HZ) can be described as the region that connects the river  
47 channel and adjacent aquifer, and includes riverbed and riverbanks. Mixing of  
48 different water types (groundwater, surface water) and ages in the HZ causes spatially  
49 and temporally varying exchange of water, biogeochemical species, and energy  
50 between river channel, riverbed and aquifer (Cardenas, 2009b; Hester and Gooseff,  
51 2010; Krause et al., 2011, 2017, 2022; McClain et al., 2013; Boano et al., 2014).  
52 Hyporheic exchange flow in vertical (e.g., bedform-driven) and horizontal (e.g.,  
53 meander-driven) ~~directions~~ can add to general regional groundwater ~~upwelling or~~  
54 ~~downwelling~~, with HEF representing those surface flow components that penetrate  
55 and transport through the hyporheic sediment and back into the stream. The  
56 distribution of hyporheic flow paths strongly determines the spatial and temporal  
57 distribution of biochemical characteristics of water within the riverbed and the wider  
58 river corridor as well as the formation of so-called hot zones and hot moments  
59 (Krause et al., 2013, 2017; Cardenas, 2015; Pinay et al., 2015).

60 Hyporheic exchange flux (HEF) is controlled by parameters such as stream  
61 discharge dynamics, recharge, riverbed and aquifer hydraulic properties, local  
62 ~~pressure~~ head fluctuations, and river geometry and morphology including sinuosity  
63 and riverbank slope (Larkin and Sharp, 1992; Gomez-Velez et al., 2012; 2017;  
64 Schmadel et al., 2016). For example, Cardenas et al. (2004) ~~demonstrate~~  
65 characteristics and especially heterogeneity could increase the hyporheic exchange  
66 intensity by 17% to 32%. As such, to be able to better estimate the relative importance  
67 of HEF on catchment water fluxes and biogeochemistry requires a good  
68 understanding of the ~~interactions of its~~ different drivers and controls. This is  
69 imperative as the spatiotemporal evolution of HEF paths, the resulting change in HZ  
70 ~~extent~~ (area) and thus also the mean residence time (RT) of the exchanged water in  
71 the HZ have significant impact on flow dynamics and transient storage along the river



72 continuum and in turn control attenuation capacity (Weatherill et al., 2018) and  
73 biogeochemical functions of river corridors (Bertrand et al., 2012; Boulton et al., 2010;  
74 Brunke and Gonser, 1997).

75 Both lateral exchange between river flood-plain, as well as  
76 bedform-induced vertical exchange at the streambed interface have been found to be  
77 crucial with regards to HEF and the biogeochemical transformation potential along  
78 the river corridor (Boano et al., 2010, 2014; Gomez-Velez and Harvey, 2014;  
79 Gomez-Velez et al., 2015, 2017; Kiel and Cardenas, 2014; Stonedahl et al., 2013).

80 ~~Considerable progress has been made in our understanding of how river platform~~  
81 ~~geometry (Boano et al., 2006, 2010; Cardenas 2006; 2008; 2009a, 2009b; Stonedahl~~  
82 ~~2013), dynamic flood events (Gomez-Velez et al., 2012; 2017) and evapotranspiration~~  
83 ~~(Kruegler et al., 2020) control HEF.~~ Focusing on lateral exchange flow processes,

84 Cardenas (2008; 2009a, 2009b) developed numerical models to investigate HEF and  
85 residence time distribution (RTD) for various river channel morphologies and regional  
86 groundwater flow conditions. Their simulations indicate that channel morphology,  
87 represented by sinuosity, is a dominant factor controlling HEF, the total HZ area, and  
88 RTD. In addition, Boano et al. (2010) used a similar modeling framework to study the

89 relationship between RTD and biogeochemical transformation by introducing surface  
90 water as a major source of dissolved organic matter that triggers a sequence of redox  
91 reactions within the HZ. Reactive transport simulations showed a good relationship  
92 between RTD and denitrification reaction potential. Based on these studies,  
93 Gomez-Velez et al. (2012) conducted numerical simulations to investigate the impact


94 of aquifer parameters (water table gradient, hydraulic conductivity, dispersivity) and  
95 channel sinuosity on HEF and RTD. By comparing RTD with the timescale of nitrate

96 forming or reducing reactions, a meander can be classified as a source or sink of  
97 nitrate for (de)nitritification activities. More recent modeling studies have focused  
98 predominantly on the effects of dynamic river/groundwater stage fluctuations on  
99 lateral (e.g., Schmadel et al., 2016; Gomez-Velez et al., 2017) and vertical (e.g., Singh



---


100 et al., 2019, 2020; Wu et al., 2018, 2020, 2021) hyporheic exchange and RTD. For  
101 example, Gomez-Velez et al. (2017) explored the HZ response to a dynamic river  
102 stage under different parameter values for hydraulic conductivity, river stage during  
103 flood events, groundwater gradient and river sinuosity conditions. Their results  
104 indicate that the dynamic forcing greatly influences net HEF, the area of HZ and RTD  
105 across different scenarios, whereby higher aquifer transmissivity will likely result in a  
106 stronger but shorter response of HEF and RTD to a flood event.



107         Although there is a considerable body of numerical research on the lateral  
108 hyporheic response to the various geometrical (e.g., geometry of river channel, river  
109 slope, etc) and dynamic drivers (e.g., fluctuation of river/groundwater, gaining and  
110 losing conditions of groundwater, etc), many HZ studies do not specifically consider  
111 floodplain-driven processes or they apply vertical riverbanks with straight river  
112 planimetry in an attempt to reduce model complexity in line with the analytical or  
113 numerical solutions used (Cooper and Rorabaugh, 1963; Hunt, 1990; Schmadel et al.,  
114 2016; Gomez-Velez et al., 2017;). However, riverbanks are usually  rather than  
115 vertical (Liang et al., 2018) as they undergo erosion (Osma and Thorne, 1988).  
116 Previous research has proven that bank erosion and bank collapse are globally  
117 spreading processes controlled by various factors, such as initial bank slope angle  
118 (Zingg, 1940; Lindow et al., 2009), surface flow forces (Hagerty et al., 1995; Fox and  
119 Wilson, 2010), vegetation cover (Mayor et al., 2008; Gao et al., 2009; Puttock et al.,  
120 2013) and sediment properties (Millar and Quich, 1993). Neglecting bank slope in  
121 analytical and numerical model solutions may therefore have a significant influence  
122 on the prediction accuracy of HEF (Doble et al. 2012a, 2012b) and RTD (Derx et al.,  
123 2014; Siergieiev et al., 2015). Thus, a detailed analysis of the floodplain drivers of  
124 HEF should require a more detailed consideration of the floodplain geometry  
125 including riverbank slope in bank storage conceptual models (Sharp, 1977).

126         Few previous studies have used numerical modeling where the model is  
127 bounded by a sloping riverbank to assess the influence of bank slope on HEF for a





128 vertical section of an alluvial aquifer. In such cases, the aquifer was considered  
129 variably saturated, homogenous, and isotropic, while flow in the unsaturated zone was  
130 calculated using the Richards equation (Li et al., 2008; McCallum et al., 2010; Doble  
131 2012a; b). These studies have confirmed that neglecting bank slope can lead to an  
132 underestimation of the bank storage volume as well as the temporal HEF in vertical  
133 cross-sectional profiles, especially under relatively small bank angles. 

134 In turn, river sinuosity and ambient groundwater gradient (along the river  
135 channel) have not been studied as potential drivers of sinuosity-driven lateral HEF  
136 and RTD and their biogeochemical implications under complex riverbank   
137 morphological conditions and it needs to be determined whether considering both  
138 drivers can lead to significantly different findings as compared to previous  
139 cross-sectional profile models (Doble et al., 2012; Siergieiev et al., 2015; Derx et al.,  
140 2014). In this study, we therefore quantify the effect of bank slope on the ~~simulated~~  
141 spatial extent (area) of the HZ in sinuosity-driven river meanders and how it impacts  
142 the evolution of HEF and RTD under varying aquifer transmissivity conditions to  
143 better understand lateral HEF through the alluvial plain. We build on the numerical  
144 model introduced by Gomez-Velez et al. (2017) and consider lateral bank slope by  
145 using a deformed geometry method (DGM) approach. For this, we couple DGM with  
146 the Boussinesq equation, the vertically integrated solute transport equation and  
147 residence time distribution equation to study HEF. Our results will help to reveal the   
148 importance of bank slope for the prediction of HEF and RTD in sinuosity-driven  
149 meandering rivers.


150



---

## 151 2. Methodology

### 152 2.1 Model setup with deformed geometry method

153  Our modeling approach builds on the work of Gomez-Velez et al. (2017), who  
154 developed a comprehensive simulation tool in dimensionless form that can represent  
155 most riverbank-aquifer situations and dynamic flood conditions. In our study, we use  
156 their model as a baseline with the same equations and metrics. Additional information  
157 regarding implementation of this baseline model can be found in the SI and  
158 Gomez-Velez et al. (2017). However, where Gomez-Velez et al. (2017) assume a  
159 vertical riverbank, we consider a sloping riverbank and use the DGM approach to  
160 capture the dynamic evolution of the SWI along the river course. A constant sloping  
161 angle ( $\delta$  [°]) along the alluvial riverbank of a sinusoidal river was implemented in our  
162 model (see blue lines of conceptual model in Figure S1 and the corresponding  
163 mathematical model in Figure S2a) while the SWI was assumed to be always vertical  
164 (vertical solid red and green lines in Figure S2c). As such, the contraction or  
165 expansion of the simulated domain, i.e., displacement of the SWI can be characterized  
166 by the sloping angle (there is no movement of the SWI for the vertical riverbank case)  
167 and river stage. As the river stage changes, so does the location of the SWI.

168 When the river stage changes in our model, the sinusoidal boundary will  
169 migrate towards or away from the floodplain meaning that the submerged part of the  
170 riverbank is considered contracted and our model only considers the alluvial aquifer  
171 that is not submerged. The evolution of the SWI during a flood event can be  
172 calculated by considering river stage and bank slope via:

$$173 \quad Y(x, t) = Y_0(x) + M(t) \quad (1)$$

174 where  $Y(x, t)$  [L] is the location of the SWI boundary;  $Y_0(x)$  [L] is the initial location  
175 of the SWI. In contrast to Gomez-Velez et al. (2017), the displacement of the SWI



176 caused by the deformation of the model domain ( $M(t) = [h(t) - h(0)]/\tan(\delta)$ , where  $h(t)$   
177 [L] is transient hydraulic head) is added in Eq. (1), which represents the displacement  
178 of the river boundary in  $y$ -direction due to river stage fluctuation and bank slope angle  
179 (see the horizontal distance between the vertical red and green solid line in Figure  
180 S2c).

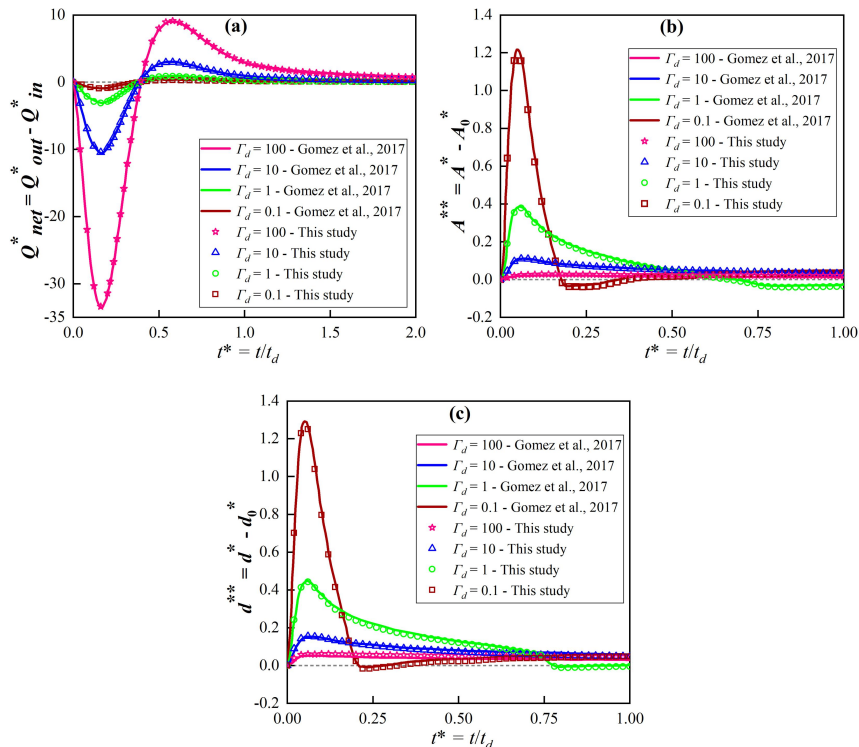
181 To simulate the model domain deformation and mesh displacement, we use the  
182 DGM interface in COMSOL. In this interface, the deforming feature of a specified  
183 domain can be defined as a boundary condition with a given moving velocity or  
184 displacement. DGM is based on the arbitrary Lagrangian–Eulerian (ALE) method,  
185 which is a hybrid method that allows both the model domain and mesh to move or  
186 deform simultaneously in a predefined manner. More details on ALE can be found in  
187 Donea et al. (2014). While it has previously been used for simulating general  
188 free-surface problems (e.g., Duarte et al., 2004; Maury, 1996; Pohjoranta and Tenno,  
189 2011), to our knowledge, DGM has not yet been implemented to solve moving  
190 boundary problems in hyporheic exchange studies. Here we used Eq. (1) as an input  
191 to the DGM interface to simulate the displacement of the SWI (water flow) during a  
192 dynamic flood event. Infiltration and seepage face before and after the peak time of  
193 the flood event, respectively, were neglected. Additionally, solute transport and RTD  
194 were simulated based on the extent of the flow field according to Gomez-Velez et al.  
195 (2017), as shown in the SI.

## 196 2.2 Model parameterization, testing and scenarios

197 Model hydraulic conditions used in our numerical modeling study are based on  
198 values from Gomez-Velez et al. (2017), who conducted a Monte Carlo analysis. They  
199 found that the dynamic variations of HEF and RTD are mainly determined by ambient  
200 groundwater flow (referred to as dimensionless parameter  $\Delta h^* = \frac{J\lambda^2}{0.5(1+n_0)H_0}$ , see Table 1)  
201 and the ratio of aquifer hydraulic conductivity to the duration of the flood event



(referred to as dimensionless constant  $\Gamma_d = \frac{S_d \lambda_z}{0.5K(1+n_0)H_0 t_d}$ , see Table 1). After setting up the original model of Gomez-Velez et al. (2017) as a baseline case ( $\delta = 90^\circ$ ), we compared our model results for that case with those obtained by Gomez-Velez et al. (2017) for (a) net HEF represented by  $Q_{net, HZ}^*(t)$ ; (b) area of HZ,  $A^{**}(t)$ ; (c) penetration of the HZ,  $d^*(t)$  in  $\Gamma_d = 0.1, 1, 10$  and  $100$ , and found that our model simulated those cases with high accuracy (Fig. 1). Parameters  $A^{**}(t)$  and  $d^*(t)$  are based on modeling the transport of a conservative solute while  $Q_{net, HZ}^*(t)$  is based on modeling water flow. Slight differences between our model and that of Gomez-Velez et al. (2017) might be due to the use of a much more refined mesh in this study and different length scales.



213

214

215 **Figure 1.** Comparison of results obtained in this study with those of Gomez et al.  
 216 (2017) for the baseline case with a vertical river bank and variable  $\Gamma_d$ : (a) net



217 hyporheic exchange flux represented by  $Q_{net, HZ}^*(t)$ ; (b) extent of the hyporheic zone  
218  $A^{**}(t)$  and (c) penetration distance  $d^*(t)$  of the hyporheic zone into the alluvial valley.  
219 A more refined mesh and different length scales used in this study, can explain  
220 occasional slight differences between our model and that of Gomez et al. (2017)  
221 might occur. Information regarding model fits can be found in the SI.

222

223 We then considered a series of riverbank scenarios where the bank slope angle  
224 ranged from  $\delta = 90^\circ$  (vertical riverbank) to  $10^\circ$  (nearly horizontal case) and  $\Gamma_d$  values  
225 ranged from 0.1 to 100, (corresponding to aquifer hydraulic conductivity ranging  
226 from 480 to 0.048 m/d, indicating high to low transmissivity. Table 1 presents the  
227 parameters used in our numerical modeling study. The finite-element models  
228 proposed in this study were developed using the COMSOL Multiphysics (COMSOL)  
229 software. Eq. (S1), Eq. (S3) and Eq. (S6) were implemented by customizing a PDE  
230 interface to include the Boussinesq, vertical integrated solute transport and RTD  
231 equation, respectively. The model domain was discretized into about 0.5 million  
232 variably-sized triangular elements, with refinement imposed near the river boundary.  
233 Mesh-independent numerical solutions are achieved by limiting grid size ( $\Delta L$ ) to less  
234 than 0.2 m. Thus, the transverse and longitudinal Peclet numbers (calculated by  $P_e =$   
235  $\Delta L/\alpha_L$  and  $P_e = \Delta L/\alpha_T$ , respectively) in both advection and diffusion dominated zones  
236 are less than 1, which is smaller than the upper limit of  $P_e = 4$  to effectively avoid  
237 numerical oscillations and instabilities.

238

239 **Table 1.** Parameters and values used in our numerical model simulations (adopted  
240 from Gomez-Velez et al. (2017)).

Parameters	Value	Description
Constant model parameters		
$S_y$	0.3	Specific yield [-]
$\lambda$	40	River boundary wave length [L]



$\alpha$	5	River boundary amplitude [L]
$\theta$	0.3	Efficient porosity [-]
$J_x$	0.0025	Base groundwater gradient [-]
$\sigma$	1.14	River boundary sinuosity [-]
$t_d$	10	Duration of flood event [T]
$n_d$	0.25	Skewness of flood event [-]
$t_p$	$n_d t_d$	Time to peak river stage [T]
$H_0$	1	Base river stage [L]
$n_0$	1	Intensity of flood event [-]
$\alpha_L$	2	Longitudinal dispersivity [L]
$\alpha_T$	$0.1 \alpha_L$	Transverse dispersivity [L]
Varied model parameters		
$\Gamma_d$	0.1 1 10 100	Dimensionless aquifer transmissivity [-]
$\delta$	90 70 50 20 10	Bank slope angle [°]

241

242



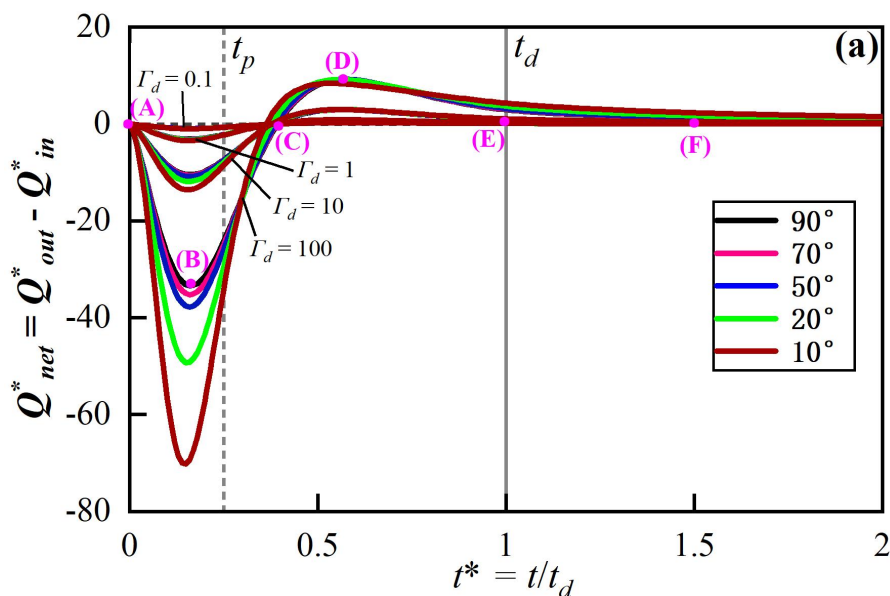
243 **3. Results**

244 **3.1 Effect of bank slope on hyporheic exchange flow and HZ patterns**

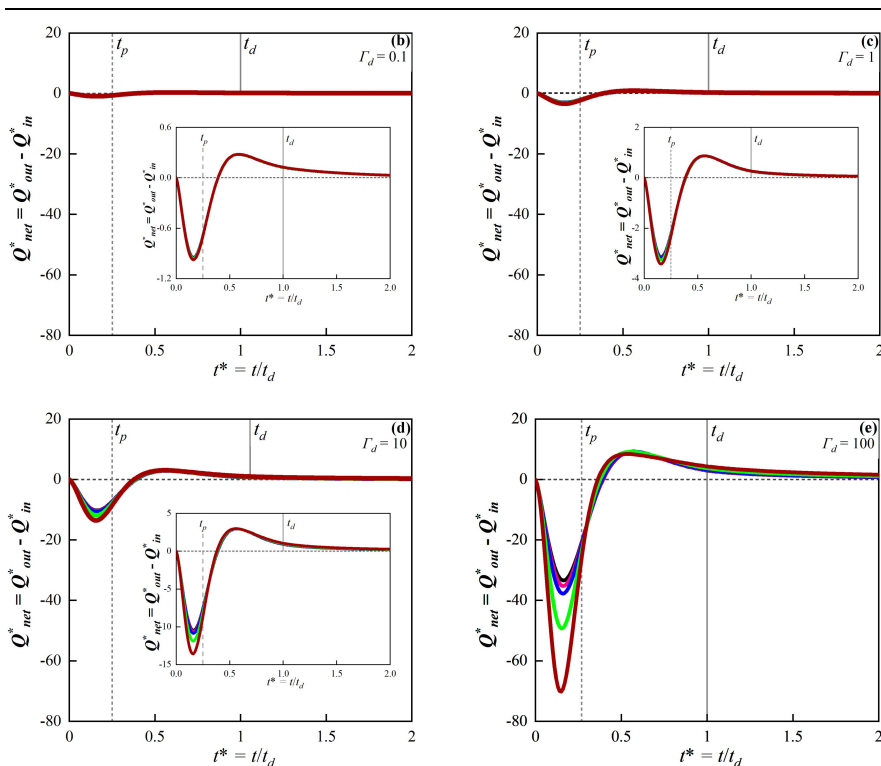
245 **3.1.1 Hyporheic exchange flow**

246 The flow field (velocity magnitude and direction) and net HEF ( $Q_{net, HZ}^*(t)$ )  
 247 changed dynamically during and after the simulated flood event. Fig. 2a shows a  
 248 comparison of  $Q_{net, HZ}^*(t)$  values for different values of  $\delta$  and  $\Gamma_d$ . In order to illustrate  
 249 the influence of  $\delta$  on  $Q_{net, HZ}^*(t)$  under different  $\Gamma_d$  conditions more clearly, Fig. 2b -  
 250 2e highlight the  $Q_{net, HZ}^*(t)$  evolution for a given  $\Gamma_d$  at smaller scale. Snapshots of the  
 251 flow field and the boundary of the HZ area (isolines of  $C(\mathbf{x}, t) = 0.5$  as concentration  
 252 of a conservative solute) for different  $\delta$  conditions at different times (pink dots in Fig.  
 253 2a) for  $\Gamma_d = 1$  are shown in Fig. 3a - 3f.

254



255



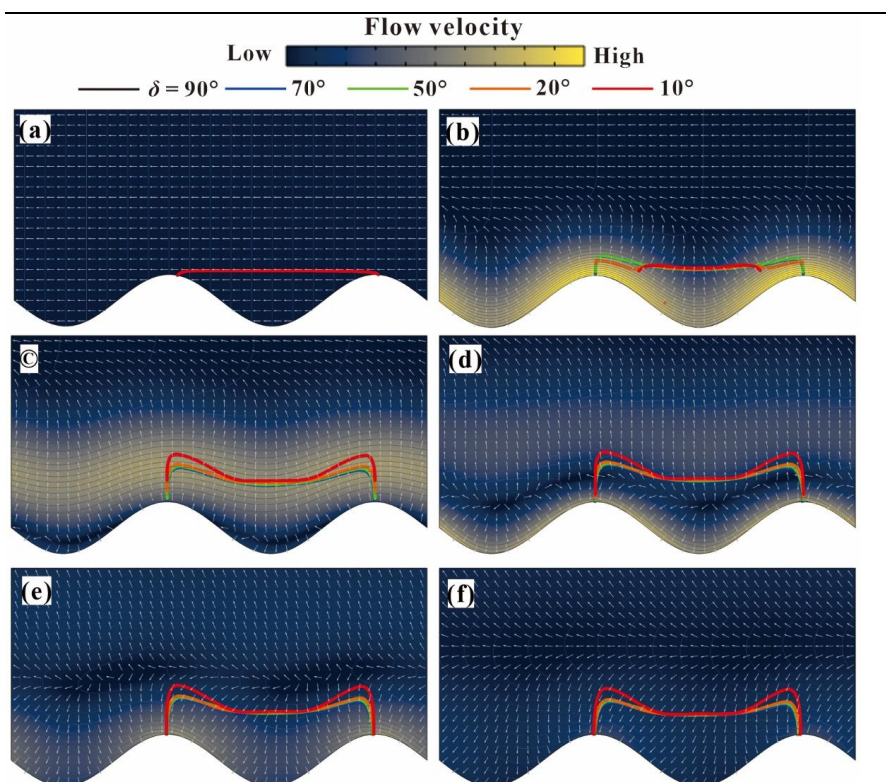
256

257

258 **Figure 2.** (a) Temporal evolution of dimensionless net flux for alternative values of  $\Gamma_d$   
 259 and  $\delta$  (colored lines). The results for each  $\Gamma_d$  condition from 0.1 to 100 and different  
 260 slopes are shown again in Fig. 2b - 2e separately, to represent smaller-scales. In each  
 261 figure, time-to-peak ( $t_p$ ) and flood duration ( $t_d$ ) are marked by vertical dashed lines.  
 262 Pink dots in (a) marked by (A) - (F) correspond to the snapshots of the flow field  
 263 shown in Fig. 3. A negative flux value here represents water flow from river to  
 264 aquifer.

265





266  
267 **Figure 3.** Temporal evolution of the alluvial flow field and spatial extent of the HZ.  
268 Snapshots of the flow field at different time steps during the simulated event (pink  
269 dots in Fig. 2a). Colored surfaces represent the magnitude of the Darcy flux vector  
270 (blue is low and yellow is high) and white isolines the dimensionless hydraulic head.  
271 **Bold colored lines correspond to the HZ extent for different bank slope conditions.**



272  
273 Before the flood event ( $t = 0$ ), steady state base flow conditions are assumed, as  
274 shown in Fig. 3a. The inflow and outflow (along the upstream and downstream  
275 meander bend, respectively) are in balance. The HZ boundaries for different  $\delta$   
276 conditions in Fig. 3a are the same before the flood event because the bank slope has  
277 no influence on the flow field and HZ extent. The onset of the flood event is indicated  
278 by the rising river stage and forces the river to infiltrate into the aquifer along the SWI  
279 (negative values of  $Q_{net, HZ}^*(t)$  in Fig. 2), resulting in the expanded HZ as shown in

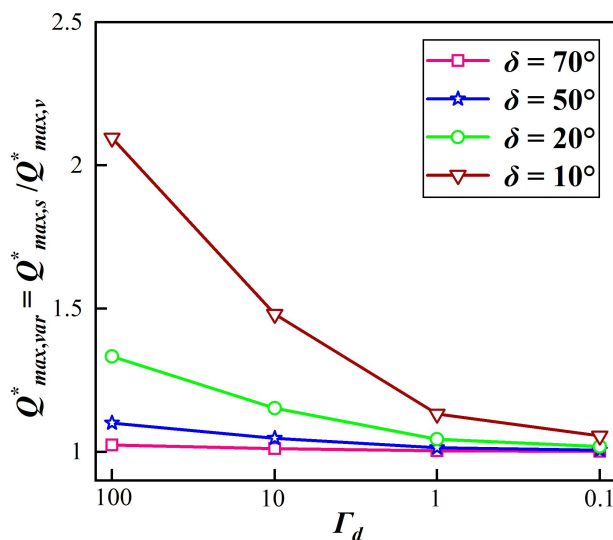


280 Fig. 3b. The influx of river water into the HZ ( $-Q_{net, HZ}^*(t)$ ) reaches its maximum  
281 before the time-to-peak river stage ( $t = 0.25t_d$ ) because the pressure wave propagates  
282 into the aquifer and decreases the head gradient between the river and the connected  
283 aquifer. An aquifer with larger  $\Gamma_d$  limits the propagation of the pressure wave due to  
284 the low transmissivity, which leads to a larger head gradient near the SWI. This,  
285 consequently, leads to larger dimensionless net fluxes under increasing  $\Gamma_d$  conditions.

286 The maximum dimensionless flux ratios  $Q_{max, var}^* = Q_{max, s}^* / Q_{max, v}^*$  of sloping ( $\delta$   
287  $< 90^\circ$ ,  $Q_{max, s}^*$ ) and vertical ( $\delta = 90^\circ$ ,  $Q_{max, v}^*$ ) riverbank cases are shown in Fig. 4. The  
288 bank slope is found to increase the infiltration flux by up to 120% ( $Q_{max, var}^* \approx 2.2$ ) for  
289  $\Gamma_d = 100$  with  $\delta = 10^\circ$  while for larger slope angles or smaller  $\Gamma_d$  the dimensionless  
290 infiltration flux gradually decreases. This is because aquifers with smaller  $\Gamma_d$  (higher  
291 hydraulic transmissivity) are more sensitive to river stage variation and have a strong  
292 ability to transmit the pressure wave into the aquifer. In such cases, the influence of  $\delta$   
293 on the net flux becomes less important. On the other hand, a smaller  $\delta$  induces a  
294 longer displacement of the SWI ( $M(t)$ ) away from the river, where the groundwater  
295 head adjacent to the SWI is always relatively low (i.e., the head in base flow  
296 condition).

297

298



299

300 **Figure 4.** Ratio of maximum negative net flux of slope to no-slope (vertical river  
 301 bank) conditions  $Q^*_{max,var} = Q^*_{max,s} / Q^*_{max,v}$ , and aquifer transmissivities. The ratios of  
 302 alternative slope condition are marked by different symbols and colors.

303

304 As the river stage decreases after  $t_p$ , the head gradient near the SWI gradually  
 305 reverses and the net outflux starts increasing (the river is gaining water). This is  
 306 associated with the river stage declining below the **gwc** groundwater level (see Fig. 3c - 3f).

307 Fig. 2 shows that the bank slope has little impact on the net outflux. Where  $\Gamma_d = 100$ ,

308 bank slope can slightly extend the time required for the system to recover to initial

309 condition after  $t_p$  but in general, the response of the net outflux to bank slope is

310 negligible when compared to that of the influx. Eventually, the net flux converges to

311 zero, which indicates the flow field within the aquifer recovers to the initial

312 conditions.

### 313 3.1.2 Patterns of hyporheic area and penetration distance

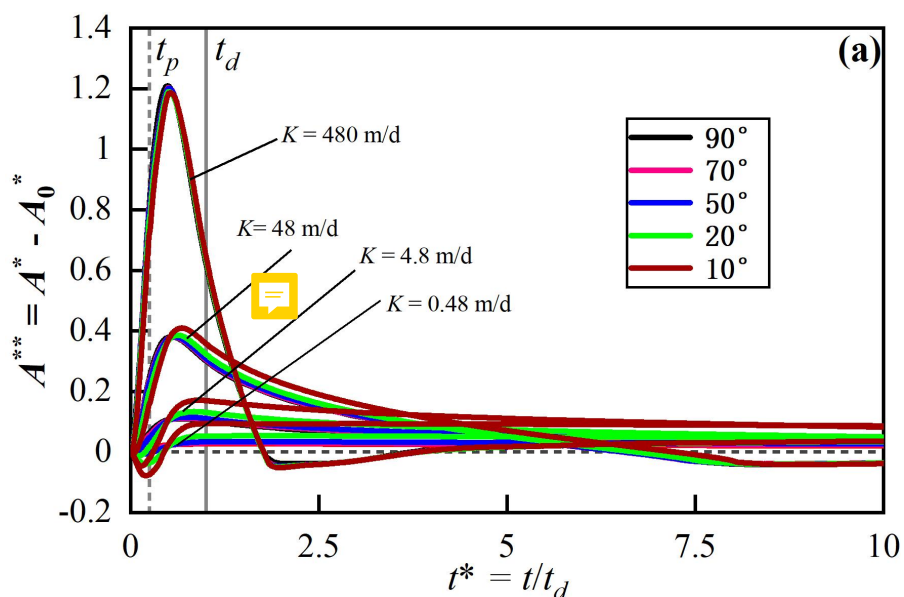
314 Fig. 5a and Fig. 6a show the temporal evolution of the HZ area ( $A^{**}(t)$ ) and

315 penetration distance ( $d^{**}(t)$ ) into the alluvial valley relative to the initial condition for

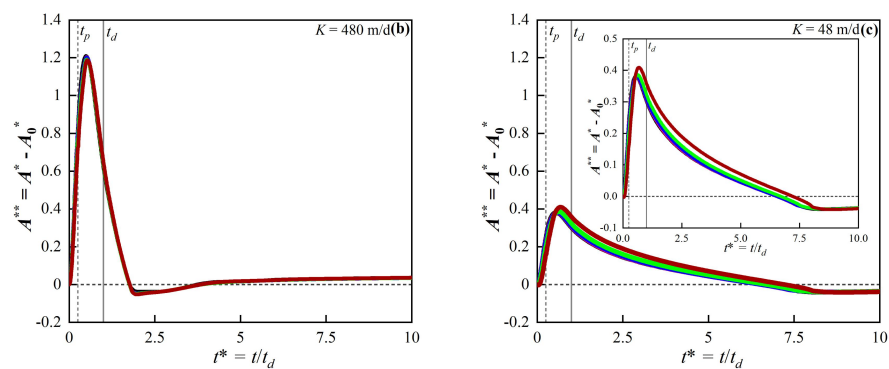


316 varying  $\Gamma_d$  and slope angles, while Fig. 5b – 5e and Fig. 6b – 6e illustrate the impact  
 317 of  $\delta$  on  $A^{**}(t)$  and  $d^{**}(t)$  for different values of  $\Gamma_d$  in a close-up.

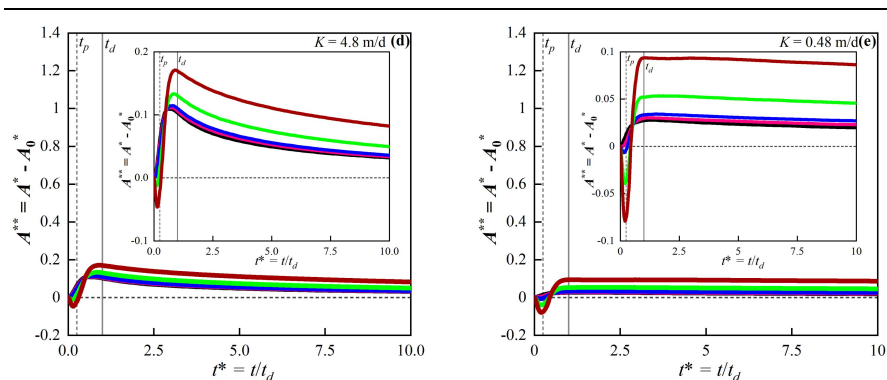
318



319



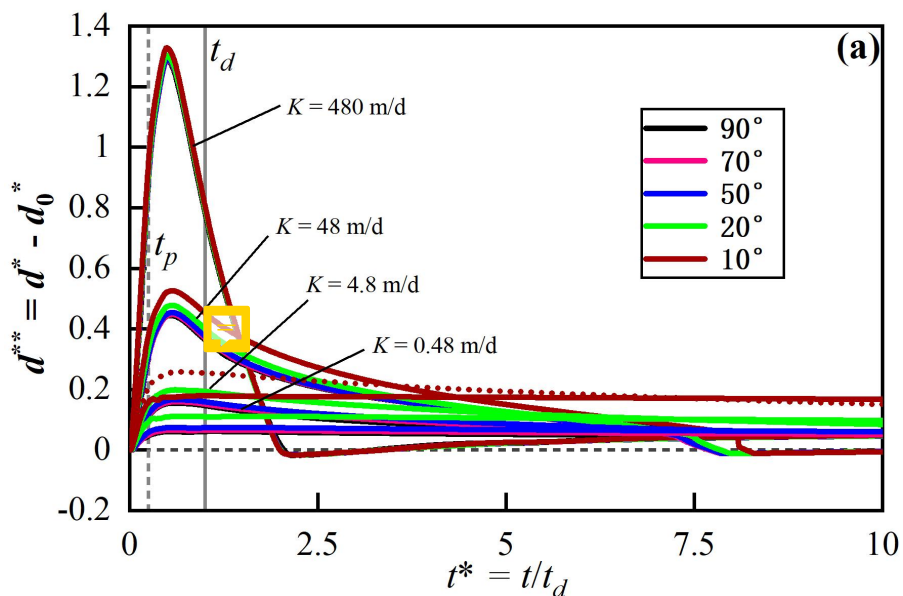
320



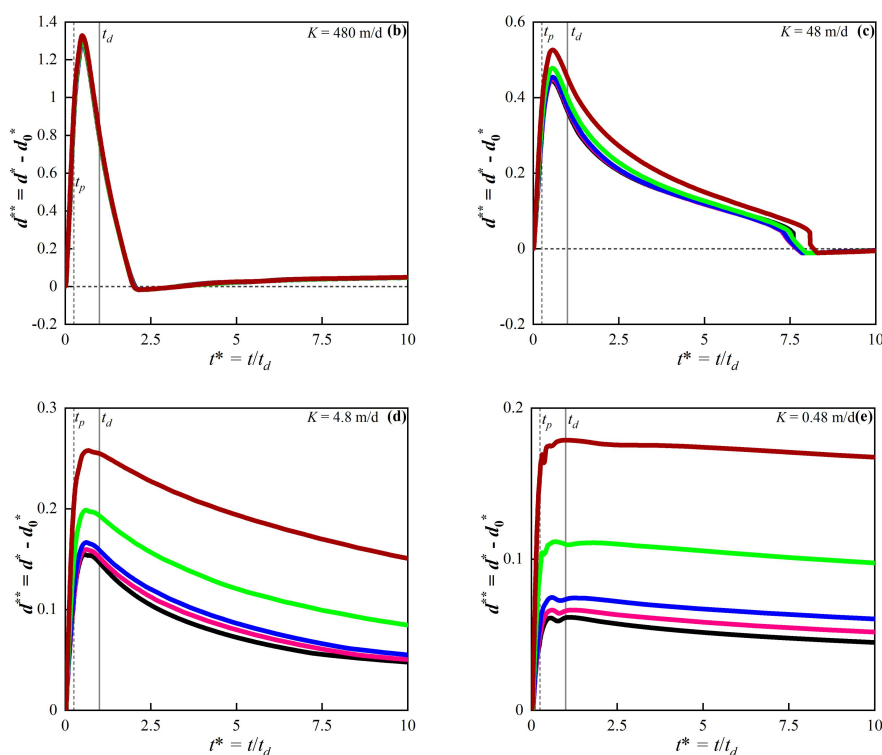
321

322 **Figure 5.** (a) Temporal evolution of HZ area for different values of  $\Gamma_d$  and  $\delta$  (colored  
 323 lines). For clarity, the results for each  $\Gamma_d$  condition from 0.1 to 100 are shown again  
 324 separately in (b) to (e), with inserts representing smaller scales.

325



326



327

328

329 **Figure 6.** (a) Temporal evolution of HZ penetration distance into the alluvial valley  
 330 for alternative values of  $\Gamma_d$  and  $\delta$  (color lines). For clarity, the results for each  $\Gamma_d$   
 331 condition from 0.1 to 100 are shown again in (b) to (e), with inserts representing  
 332 smaller scales.

333

334 For vertical banks ( $\delta = 90^\circ$ , grey lines in Fig. 5),  $A^{**}(t)$  increases synchronously  
 335 with the river stage ( $t < t_p$ ). After the peak time of the flood event ( $t > t_p$ ),  $A^{**}(t)$   
 336 continues to rise due to the water in the river still discharging into the aquifer.  
 337 Furthermore, the groundwater mound continues to expand, migrating into the aquifer  
 338 (see the more penetrated groundwater mound from in Fig. 3b vs Fig. 3c). After the  
 339 flood event ( $t > t_d$ ), the river water that was stored in the aquifer ( $C(x, t) > 0$ ) slowly  
 340 discharges back into the river channel. Thus, the HZ area and penetration distance  
 341 gradually rebound to initial conditions.



342 Under sloping riverbank conditions, the riverbank will at times be submerged  
343 by the rising river stage. Fig. 5b and 6b show that the effects of bank slope on  $A^{**}(t)$   
344 and  $d^{**}(t)$  are almost counteracted by the high transmissivity of the aquifer and the  
345 influence of bank slope on HZ area and penetration distance is negligible. At the  
346 beginning of the flood event, Fig. 5c - 5e show that for conditions with smaller  $\delta$ ,  
347  $A^{**}(t)$  can be less than zero (HZ at these times are smaller than the initial condition).  
348 This is due to the fact that the movement of the SWI during a rising river stage  
349 towards the alluvial valley will submerge parts that were previously unsaturated as the  
350 aquifer with low transmissivity will propagate water more slowly. As  $\Gamma_d$  increases  
351 from Fig. 5d - 5e, smaller values of  $A^{**}$  were observed that stay negative for a longer  
352 time for smaller bank slopes  $\delta$ . This indicates that the bank slope has a more  
353 significant effect on HZ area in cases where  $\Gamma_d$  is large as a low-transmissivity aquifer  
354 takes more time to propagate infiltrating river water.

355 After about half of the flood duration ( $t > 0.5t_d$ ), all of  $A^{**}(t)$  becomes positive  
356 due to the re-emergence of the model domain submerged during the flood event. As  $\Gamma_d$   
357 increases from Fig. 5b - 5e and from Fig. 6b - 6e, the impact of  $\delta$  gradually emerges  
358 especially in larger  $\Gamma_d$  condition, whereby smaller  $\delta$  can increase the peak values of  
359  $A^{**}(t)$  and  $d^{**}(t)$ , and delay the arrival time of the maximum value of  $A^{**}(t)$ . After the  
360 flood event ( $t > t_d$ ), the effect of bank slope is counteracted by the higher aquifer  
361 transmissivity and only for large transmissivities has a significant impact on the HZ  
362 resulting in larger  $A^{**}(t)$  and  $d^{**}(t)$  as shown in Fig. 5c - 5e and Fig. 6c - 6e.

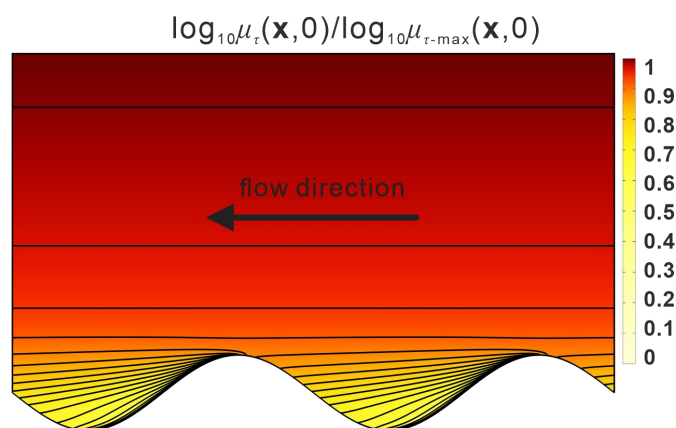
### 363 3.2 Spatiotemporal evolution of mean residence time distribution

364 The evolution of spatiotemporal patterns of mean RTD is a useful evaluation  
365 method for identifying the dynamic variation of aging and rejuvenation of hyporheic  
366 water. Here we use the mean RT ratio between a sloping model and a vertical model  
367  $\mu_r^*(\mathbf{x}, t) = \log_{10}(\mu_{r-s}(\mathbf{x}, t)/\mu_{r-v}(\mathbf{x}, 0))$  to evaluate the influence of bank slope on the  
368 predicted RTD for a given location and time. Fig. 7 presents RTDs for the initial



369 condition, where  $\mu_{t_0-\max}$  is the maximum RT in the domain. It can be seen that the  
370 isolines representing the RT are almost horizontal in the area extending from the river  
371 but RT near the upstream river bend is smaller than downstream because the initial  
372 flow direction is towards the negative direction of the  $x$  axis. Notably,  $\mu(\mathbf{x}, 0)$  grows  
373 almost exponentially as  $y$  increases, and a positive correlation to  $\Gamma_d$  at a given location  
374 is observed.

375



376

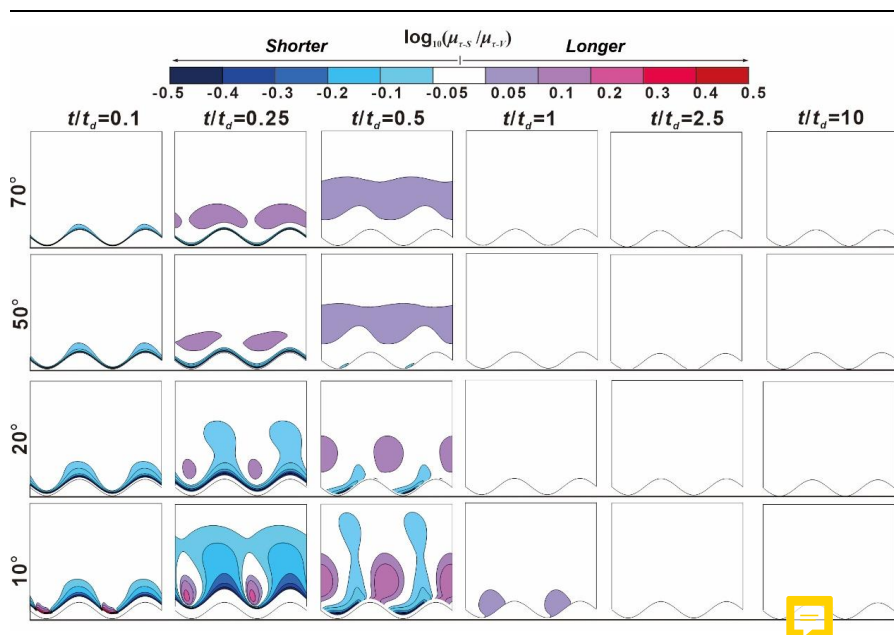
377 **Figure 7.** Relative mean residence time distributions [-] for baseline flow conditions  
378 (no slope), which are represented by  $\log_{10}\mu_t(\mathbf{x}, 0)/\log_{10}\mu_{t-\max}(\mathbf{x}, 0)$  to show the  
379 distribution pattern. The value of the contour lines grows exponentially with the  
380 distance from the river meander.

381

382 Fig. 8 - 11 present snapshots of  $\mu_r^*$  for different bank slopes for  $\Gamma_d = 0.1, 1, 10$   
383 and 100, respectively, at the rising limb of the flood event ( $t/t_d = 0.1$ ), the peak of  
384 flood event ( $t/t_d = 0.25$ ), the falling limb of flood ( $t/t_d = 0.5$ ) and after the flood event  
385 ( $t/t_d = 1, 2.5$  and 10). The RT difference between sloping and vertical riverbank  
386 models are within 12.2% in the white-colored areas ( $-0.05 < \mu_r^* < 0.05$ ) of Fig. 8 - 11,  
387 which indicates a minor effect of bank slope on RTD.

388

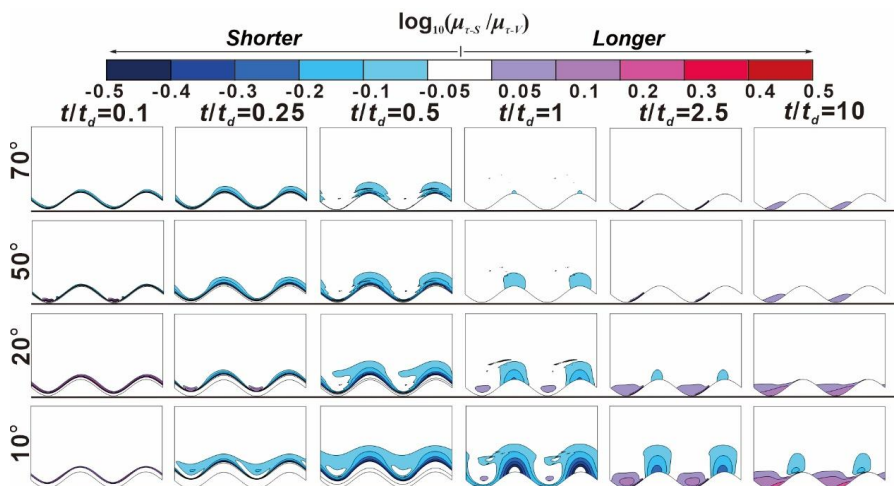




389

390 **Figure 8.** Snapshots for the RTD ratio  $\mu_r^*(x, t)$  between sloping and vertical riverbank  
 391 conditions at different times  $t/t_d$  as a function of  $\delta$  for  $\Gamma_d = 0.1$ . The horizontal lines  
 392 beneath each figure are the reference lines to show the initial location of SWI. The  
 393 lower sinuous lines at the reference lines are the initial SWIs.

394



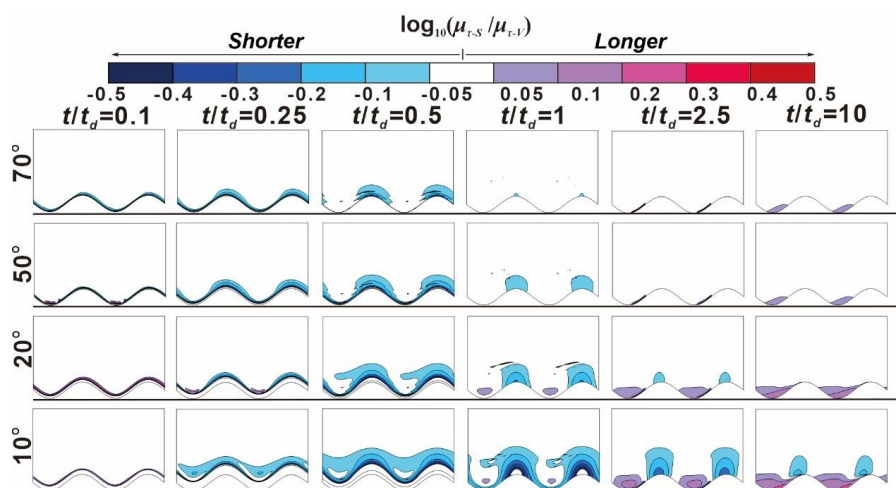
395

396 **Figure 9.** Snapshots for the RTD ratio  $\mu_r^*(x, t)$  between sloping and vertical riverbank  
 397 conditions at different times  $t/t_d$  as a function of  $\delta$  for  $\Gamma_d = 1$ . The horizontal lines



398 beneath each figure are the reference lines to show the initial location of SWI. The  
399 lower sinuous lines at the reference lines are the initial SWIs.

400



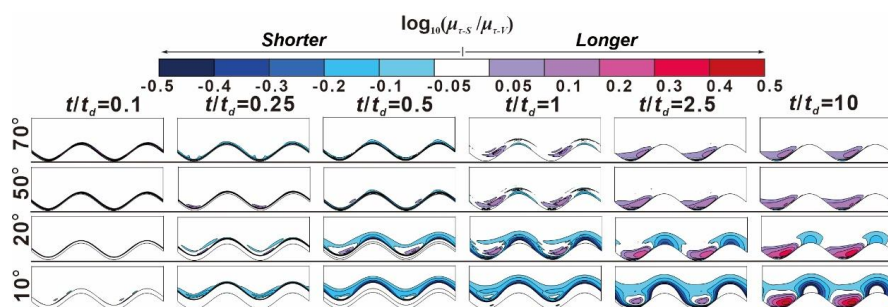
401

402 **Figure 10.** Snapshots for the RTD ratio  $\mu_r^*(x, t)$  between sloping and vertical  
403 riverbank conditions at different times  $t/t_d$  as a function of  $\delta$  for  $\Gamma_d = 10$ . The  
404 horizontal lines beneath each figure are the reference lines to show the initial location  
405 of SWI. The lower sinuous lines at the reference lines are the initial SWIs.

406



407



408

409 **Figure 11.** Snapshots for the RTD ratio  $\mu_r^*(x, t)$  between sloping and vertical  
 410 riverbank conditions at different times  $t/t_d$  as a function of  $\delta$  for  $\Gamma_d = 100$ . The  
 411 horizontal lines beneath each figure are the reference lines to show the initial location  
 412 of SWI. The lower sinuous lines at the reference lines are the initial SWIs.

413

414 At  $t/t_d = 0.1$ , a smaller bank slope can lead to shorter RT (negative values of  $\mu_r^*$ )  
 415 near the SWI. The area of shorter RT caused by bank slope was positively related to  
 416 aquifer transmissivity. The effect of  $\delta$  is small for  $\Gamma_d = 10$  and 100 because the  
 417 groundwater mound piles up around the river boundary, but that small area extended  
 418 deeper into the alluvial valley for smaller  $\delta$ . Due to the scattered and nested flow  
 419 paths near the inner bend (cut bank) and outer bend (point bar), respectively, the  
 420 penetration distance of the negative value of  $\mu_r^*$  area at the cut bank of SWI is larger  
 421 than that at the point bar. The change of flow direction near the point bar leads to a  
 422 prolonged flow path for the water in the river as well as to forced groundwater mixing  
 423 with the slightly older water. This effect was amplified with decreasing bank slope,  
 424 but it is only statistically significant ( $\mu_r^* < -0.05$  or  $\mu_r^* > 0.05$ ) when  $\delta = 10^\circ$  at  $t/t_d =$   
 425 0.1.

426 At the time of peak flood ( $t/t_d = 0.25$ ), the river still infiltrates into the aquifer.  
 427 For  $\Gamma_d = 0.1$ , bank slope can lead to both younger and older water, i.e., water  
 428 undergoing shorter and longer RT. Both magnitude of  $\mu_r^*$  and associated RT area  
 429 increase with decreasing slope due to the longer penetration distance of river water





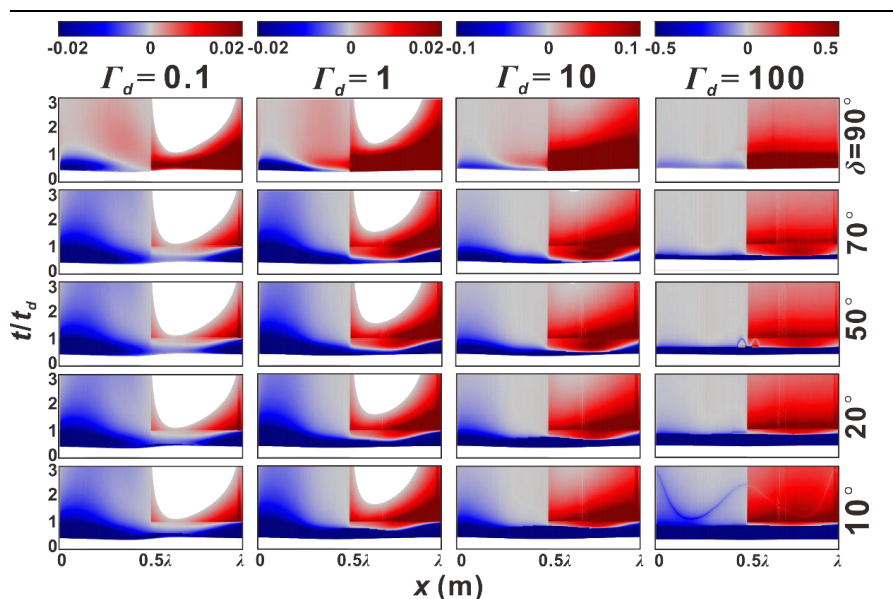
430 into the aquifer. As  $\delta$  decreases, the positive values of  $\mu_r^*$  are located closer to the  
431 downstream point bar. The impact of bank slope on RTD for  $\Gamma_d = 1$  is rather similar in  
432 its pattern compared to  $\Gamma_d = 0.1$ , but  $\mu_r^*$  was significant only for  $\delta = 10^\circ$ . For  $\Gamma_d = 10$   
433 and 100, the effect of bank slope can lead to larger and deeper penetration of the river  
434 water into the alluvial valley (Fig. 8 - 11) but this effect is smaller than when looking  
435 at smaller  $\Gamma_d$  because of the lower hydraulic transmissivity.

436 At  $t/t_d = 0.5$ , part of the submerged aquifer at  $t/t_d = 0.25$  reemerges due to the  
437 decline in river stage. In most cases, smaller bank slopes can lead to wider  
438 reemergence of the aquifer, and therefore result in smaller  $\mu_r^*$  near the river boundary;  
439 however, this is not the case for  $\Gamma_d = 0.1$  where bank slope can both increase and  
440 decrease the RT of pore water. Furthermore, compared to when  $t/t_d = 0.25$ , the impact  
441 of bank slope becomes weaker for  $\Gamma_d = 0.1$ , but more relevant for the larger  $\Gamma_d$  values.

442 After the flood event ( $t/t_d > 1$ ), the influence of bank slope on RT is nearly  
443 eliminated for  $\Gamma_d = 0.1$  and 1 due to the high aquifer transmissivity. However, for  
444 aquifers with lower transmissivity ( $\Gamma_d = 10$  and 100), bank slope still has a significant  
445 effect on RT at  $t/t_d = 10$  and leads to older water near the point bar, which indicates  
446 the bank slope has a more lasting influence on aquifer RT, as more time is required to  
447 recover to initial condition.

### 448 3.3 Relative flux-weighted residence time

449 Fig. 12 shows the evolution of the flux-weighted relative RT  $\mu_{out}^*(x, t) = \mathbf{n} \cdot \mathbf{Q}_{out}^*(x,$   
450  $t) \log_{10}(\mu_r(x, t) / \mu_r(x, 0))$  for different slopes and aquifer transmissivities.  $\mu_{out}^*(x, t)$   
451 represents the difference in flux-weighted RT of the water discharged into the river  
452 compared to the initial condition. At the start of the flood event, there is no  $\mu_{out}^*$  as  
453 river water infiltrates the aquifer. Following the decline in river stage, the aquifer  
454 begins to discharge the mixed water with different RT back into the river (see Fig. 3c).  
455



456

457 **Figure 12.** Temporal evolution of flux-weighted ratios of RT to the RT for base flow  
 458 condition ( $\mu^*_{out}(x, t) = \mathbf{n} \cdot \mathbf{Q}^*_{out}(x, t) \log_{10}(\mu_r(x, t)/\mu_r(x, 0))$ ) along the river meander as a  
 459 function of  $\delta$  and  $\Gamma_d$ .

460

461 For vertical riverbank conditions ( $\delta = 90^\circ$ , top row in Fig. 12), upstream ( $0.5\lambda <$   
 462  $x < \lambda$ ) and downstream ( $0 < x < 0.5\lambda$ ) boundaries of the meander bend discharge older  
 463 and younger water, respectively. The waters with relatively younger or older RT are  
 464 mostly discharged before the flood event ( $t/t_d < 1$ ) due to the greater outflux as shown  
 465 in Fig. 2a. It also can be seen that water is older along the upstream bend compared to  
 466 the more rejuvenated water along the downstream bend. After the flood event,  $\mu^*_{out}$   
 467 gradually disappears along the upstream meander (blank areas) for  $\Gamma_d = 0.1$  and 1,  
 468 because the flow fields are recovering to base flow conditions. Therefore, the  
 469 upstream meander gradually becomes the inflow boundary.

470 For cases with lower values of  $\Gamma_d$  (left columns in Fig. 12),  $\mu^*_{out}$  reaches  
 471 equilibrium earlier compared to cases with higher  $\Gamma_d$ . As  $\delta$  decreases from the top  
 472 row to the bottom row in Fig. 12, the increased impact of bank slope causes  $\mu^*_{out}$  to  
 473 gradually decrease the RT of the outflux during the flood event. For larger  $\Gamma_d$ ,  $\mu^*_{out}$  is



---

474 totally dominated by younger water during the flood event. Furthermore, the stronger  
475 impact of smaller bank slope angles can both extend the time over which and increase  
476 the magnitude with which younger water is discharging along the downstream  
477 meander.

## 478 **4. Discussion**

### 479 **4.1. Why we should account for bank slope**

480 Tilted riverbanks are common in nature and caused by erosion and bank collapse,  
481 as has been observed at multiple scales (Zingg, 1940). Previous studies have shown  
482 that bank erosion is stronger where the river planimetry is more sinuous, river stage  
483 varies more frequently, or where the riverbank has larger sloping angles, ultimately  
484 leading to a flatter bank (Zingg, 1940; Hagorty et al., 1995; Mayor et al., 2008;  
485 Puttock et al., 2013). Hence, recent studies have recognized the need for a  
486 comprehensive analysis of how riverbank topography affects lateral hyporheic  
487 exchange along meandering streams (Boano et al., 2014) and the specific importance  
488 of bank slope on hyporheic exchange has been highlighted by Doble et al. (2012) and  
489 Liang et al. (2018). Yet, in most previous studies, the impact of riverbank geometry  
490 and in particular bank slope on sinuosity-driven lateral hyporheic exchange was  
491 ignored. Flow was usually only considered perpendicular to the river axis, i.e., HEF in  
492 river flow direction caused by the alluvial valley slope and river sinuosity was not  
493 considered. However, as river planimetry can vary significantly along river corridors  
494 (Hooke, 2013; Seminara, 2006), and the alluvial valley slope has a potentially  
495 non-negligible impact on hyporheic exchange (Gomez-Velez et al., 2017), we  
496 considered it important to close this knowledge gap by specifically focusing on the  
497 impact of bank slope and the ambient groundwater gradient for various groundwater  
498 flow conditions (as manifested through aquifer transmissivity) on HEF. Our results



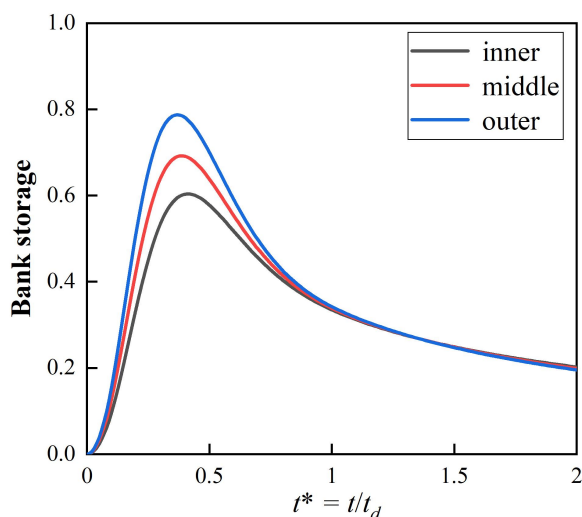
---

499 clearly indicate that HZ characteristics (flow field, area and penetration distance of  
500 HZ into alluvial valley) can significantly vary along a meandering river depending on  
501 bank slope conditions.

502 Not accounting for bank slope and river sinuosity can lead to an  
503 underestimation of infiltration from the river to the alluvial aquifer. This effect is  
504 more pronounced for smaller bank slope angles and losing conditions can be  
505 significantly underestimated. Doble et al. (2012), Siergieiev et al. (2015) and Liang et  
506 al. (2018), assessed the influence of bank slope on HEF using a vertical  
507 cross-sectional profile. Siergieiev et al. (2015) found that the impact of bank slope on  
508 HEF was proportional to the hydraulic conductivity of the aquifer. However, we argue  
509 here that bank slope is more relevant in rivers connected to aquifers with low  
510 hydraulic transmissivity. Furthermore, we show (Fig. 13) that using only one  
511 cross-sectional river profile perpendicular to the river axis does not capture the effect  
512 of river sinuosity on HEF as bank storage decreases from point bar to cut bank. That  
513 means the previous vertical cross-sectional profile models could not calculate the  
514 bank storage evolution accurately when neglecting the sinuosity of river. In a  
515 meandering river with variable bank slope, river geometry thus has a sizable effect on  
516 bank storage evolution and HEF, and should be included into the future analytical/  
517 numerical models.

518





519

520 **Figure 13.** Bank storage versus time for  $\Gamma_d = 1$  and  $\delta = 90^\circ$  condition at: inner bend  
521 ( $x = 0$ ); middle bend ( $x = 0.25\lambda$ ); outer bend ( $x = 0.25\lambda$ ). Dimensionless bank storage

522 was calculated by 
$$\frac{\int_{y(x,t)}^{y(x,t)+4\lambda} [h-z_b-H_0] dy}{\lambda H_p}$$
.

523

524 The impact of bank slope on RT is basically controlled by aquifer transmissivity.  
525 When aquifer transmissivity increases, the impact of bank slope appears to be more  
526 pronounced when river stage rises during a flood event. For decreasing aquifer  
527 transmissivity, bank slope seems more relevant for RTD after the flood event and its  
528 impact is more long-lasting. Bank slope could result in longer (near the point bar) or  
529 shorter (near the cut bank) pore water RT at various times of a flood event. This  
530 means that point bars with bank slopes are more conducive for river restoration (e.g.,  
531 removal of dissolved organic carbon) while cut banks with bank slope may have  
532 adverse effects on the groundwater quality near rivers. This is important to keep in  
533 mind when assessing the influence of bank slope on biogeochemical efficiency. For  
534 example, previous research indicates that the residence time of river water in the HZ  
535 can control, and is often proportional to nutrient cycling (McCallum and Shanafield,  
536 2016; Wondzell and Swanson, 1999; Zarnetske et al., 2011, 2012). As such, an





537 analysis of RTD can provide valuable information on whether and where riverbank  
538 slope can induce biogeochemical hotspots and hot moments and help guide choices to  
539 be made in biogeochemical field surveys regarding location and sampling time under  
540 dynamic river stage conditions, especially when the connected aquifers have low  
541 hydraulic transmissivity.

#### 542 **4.2. Advantages and limitations of using a reduced 2-D model**

543 In this study, we propose a parsimonious reduced-order, idealized horizontal  
544 2-D model that simplifies the variation of the river-aquifer interface by using the  
545 moving boundary method to depict the displacement of SWI along a sloping  
546 riverbank. An advantage of this approach is reduced model complexity as compared  
547 to a three-dimensional model, which greatly reduces time and data requirements  
548 during model building and computational demand during simulation of HEF and  
549 especially residence time distributions. Thus, our reduced-order model acts as a first  
550 step to gain insight into the patterns of hyporheic exchange, riverbank storage and  
551 RTD in settings with more complex riverbank morphology and dynamic forcing.  
552 Future efforts should be focused on optimizing the computational method applied  
553 here and on including more detailed morphology and hydrodynamic characteristics.

554 It is important to note that in our simulations we assume a constant angle of  
555 bank slope along the meandering river while natural riverbanks often have  
556 non-uniform slopes which could lead to a different behavior. Thus, new  
557 conceptualizations that account for the contribution of bank slope on time-varying  
558 RTD and HZ extent can be applied to gain better understanding of a hyporheic zone,  
559 especially in cases where bank slope is small, or where the system is relatively  
560 insensitive to changes during peak flow.

561 In our simulations we tested the model using a range of aquifer hydraulic  
562 conductivities. Although hydraulic conductivity (or transmissivity) is a critical  
563 parameter in the quantification of exchange fluxes and RTD between the two systems



564 under varying slope conditions, other parameters such as valley water head fluctuation,  
565 peak flood event characteristics or larger scale groundwater head fluctuation, e.g., due  
566 to changing groundwater recharge patterns have not been considered here but might  
567 also impact HZ extent, RTD and river-aquifer exchange flux.

568


## 569 5. Conclusions

570 The deformed geometry method was applied to characterize the expansion and  
571 contraction of hyporheic zones along sloping riverbanks, and to evaluate the impact of  
572 bank slope on hyporheic exchange flux, evolution of the HZ area and RTD. To  
573 achieve this, various alluvial aquifers with varying slope angles and aquifer  
574 transmissivity values were simulated. Our results show that bank slope in a  
575 sinuosity-driven river can have significant impact on the evolution of the hyporheic  
576 zone during and after a flood event (transient flood forcing).

577 The overall findings of our work underline the need for a detailed analysis of  
578 lateral hyporheic exchange flow responses to dynamic forcings (including the  
579 assumption of more realistic riverbank morphology conditions). Furthermore, our  
580 results show that more detailed information on bank slope (e.g., through more  
581 measurements) can lead to a better understanding of hyporheic flow patterns and  
582 potentially result in improved biogeochemical process understanding for real-world  
583 conditions in more complex morphology and depositional environments. Several  
584 conclusions can be drawn from our study:

- 585 1. Sloping riverbanks can increase HEF, especially when the river is connected to a  
586 low-transmissivity alluvial aquifer and bank slope angles are small. However,  
587 bank slope has only a minor impact on the hyporheic outflow flux.
- 588 2. During a flood event, the bank slope can increase the area and penetration distance  
589 of the HZ into the alluvial aquifer. This effect is more pronounced and



- 
- 590 long-lasting for low-transmissivity aquifers. 
- 591 3. During a flood event, the impact of bank slope on RTD is more pronounced for  
592 high transmissivity aquifers. On the contrary, the impact of bank slope on RTD for  
593 lower transmissivity aquifers is minor during the flood event, but can have a  
594 significant and long-lasting effect under post-flood conditions.
- 595 4. River sinuosity should be considered when assessing the impact of bank slope on  
596 RTD. Variable bank slope can lead to both longer and shorter RT compared to  
597 vertical riverbank conditions.
- 598 5. Bank slope has a greater impact on the residence time of hyporheic water in  
599 lower-transmissivity aquifers, thereby delaying the time of younger water  
600 discharge downstream of a meander bend, which also delays the outflow of older  
601 water upstream of that bend.



602 **Code and data availability**

603 Additional information regarding methodology and results is provided in the  
604 supporting information (SI).

605 **Author contributions**

606 YL: Conceptualization, Formal analysis, Investigation

607 US: Conceptualization, Methodology, Writing

608 ZW: Funding acquisition, Software, Supervision

609 SK: Validation, Writing, Supervision

610 HL: Project administration, Supervision

611 **Acknowledgements**

612 This research was partially supported by the National Natural Science Foundation of  
613 China (Grant Numbers: 42272290, 41830862, and 42022018), and China Scholarship  
614 Council (CSC, 202106410042).

615

616 **Competing interests**

617 The authors declare that they have no conflict of interest.



---

618 **References**

- 619 Bear, J., and Cheng, A. H. D.: Modeling groundwater flow and contaminant transport,  
620 Vol. 23, pp. 83, Dordrecht: Springer, 2010.
- 621 Bertrand, G., Goldscheider, N., Gobat, J.-M., and Hunkeler, D.: Review: From  
622 multi-scale conceptualization to a classification system for inland  
623 groundwater-dependent ecosystems, *Hydrogeology Journal*, 20, 5-25, 2012.
- 624 Boano, F., Camporeale, C., Revelli, R., and Ridolfi, L.: Sinuosity-driven hyporheic  
625 exchange in meandering rivers, *Geophysical Research Letters*, 33, L18406, 2006.
- 626 Boano, F., Harvey, J. W., Marion, A., and Packman, A. I., Revelli, R., Ridolfi, L., and  
627 Wörman, A.: Hyporheic flow and transport processes: Mechanisms, models, and  
628 biogeochemical implications, *Reviews of Geophysics*, 52, 603-679, 2014.
- 629 Boano, F., Demaria, A., Revelli, R., and Ridolfi, L.: Biogeochemical zonation due to  
630 intrameander hyporheic flow, *Water Resource. Research*. 46, W02511, 2010.
- 631 Boulton, A. J., Datry, T., Kasahara, T., Mutz, M., and Stanford, J. A.: Ecology and  
632 management of the hyporheic zone: Stream-groundwater interactions of running  
633 waters and their floodplains, *Journal of the North American Benthological*  
634 *Society*, 29 (1), 26-40, 2010.
- 635 Brunke, M., and Gonser, T.: The ecological significance of exchange processes  
636 between rivers and groundwater, *Freshwater Biology*, 37 (1), 1-33, 1997.
- 637 Cardenas, M. B.: The effect of river bend morphology on flow and timescales of  
638 surface water-groundwater exchange across pointbars, *Journal of Hydrology*, 362,  
639 134-141, 2008.
- 640 Cardenas, M. B.: A model for lateral hyporheic flow based on valley slope and  
641 channel sinuosity, *Water Resources Research*, 45, W01501, 2009a.
- 642 Cardenas, M. B.: Stream-aquifer interactions and hyporheic exchange in gaining and  
643 losing sinuous streams, *Water Resources Research*, 45, W06429, 2009b.
- 644 Cardenas, M. B.: Hyporheic zone hydrologic science: A historical account of its



- 
- 645 emergence and a prospectus, *Water Resources Research*, 51, 3601-3616, 2015.
- 646 Cooper, H. H., and Rorabaugh, M. I.: Ground-water movements and bank storage due  
647 to flood stages in surface streams, Report of Geological Survey Water-Supply, pp.  
648 1536-J, US Government Printing Office, Washington, United States, 1963.
- 649 Derx, J., Farnleitner, A. H., Blöschl, G., Vierheilig, J., and Blaschke, A. P.: Effects of  
650 riverbank restoration on the removal of dissolved organic carbon by soil passage  
651 during floods—A scenario analysis, *Journal of Hydrology*, 512, 195-205, 2014.
- 652 Doble, R. C., Crosbie, R. S., Smerdon, B. D., Peeters, L., and Cook, F. J.:  
653 Groundwater recharge from overbank floods, *Water Resources Research*, 48 (9),  
654 W09522, 2012a.
- 655 Doble, R., Brunner, P., McCallum, J., and Cook, P. G.: An analysis of river bank slope  
656 and unsaturated flow effects on bank storage, *Ground Water*, 50 (1), 77-86,  
657 2012b.
- 658 Donea, J., A. Huerta, J.-P. Ponthot, and A. Rodriguez-Ferran.: Arbitrary  
659 Lagrangian–Eulerian methods, In *Encyclopedia of Computational Mechanics*, ed.  
660 E. Stein, R. de Borst, and T. J. R. Hughes, 413-434. New York: John Wiley &  
661 Sons, 2004.
- 662 Duarte, F., Gormaz, R., and Natesan, S.: Arbitrary Lagrangian–Eulerian method for  
663 Navier–Stokes equations with moving boundaries, *Computer Methods in  
664 Applied Mechanics and Engineering*, 193 (45-47), 4819-4836, 2004.
- 665 Fox, G. A., and Wilson, G. V.: The role of subsurface flow in hillslope and stream  
666 bank erosion: a review, *Soil Science Society of America Journal*, 74 (3), 717-733,  
667 2010.
- 668 Gao, Y., Zhu, B., Zhou, P., Tang, J. L., Wang, T., and Miao, C. Y.: Effects of  
669 vegetation cover on phosphorus loss from a hillslope cropland of purple soil  
670 under simulated rainfall: a case study in China, *Nutrient Cycling in  
671 Agroecosystems*, 85 (3), 263-273, 2009.
- 672 Gomez-Velez, J. D., and Harvey, J. W.: A hydrogeomorphic river network model



- 
- 673 predicts where and why hyporheic exchange is important in large basins,  
674 Geophysical Research Letters, 41, 6403–6412, 2014.
- 675 Gomez, J. D., Wilson, J. L., and Cardenas, M. B.: Residence time distributions in  
676 sinuosity - driven hyporheic zones and their biogeochemical effects, Water  
677 Resources Research, 48 (9), 2012.
- 678 Gomez-Velez, J. D., Wilson, J. L., Cardenas, M. B., and Harvey, J. W.: Flow and  
679 residence times of dynamic river bank storage and sinuosity-driven hyporheic  
680 exchange, Water Resources Research, 53, 8572-8595, 2017.
- 681 Gomez-Velez, J. D., Harvey, J. W., Cardenas, M. B., and Kiel, B.: Denitrification in  
682 the Mississippi River network controlled by flow through river bedforms, Nature  
683 Geoscience, 8, 941-945, 2015.
- 684 Hagerty, D. J., Spoor, M. F., and Parola, A. C.: Near-bank impacts of river stage  
685 control, Journal of Hydraulic Engineering, 121 (2), 196-207, 1995.
- 686 Hooke, J. M.: River meandering, In E. Wohl & J. Shroder (Eds.), Treatise on  
687 geomorphology, Vol. 9, pp. 260-288, CA: Academic Press, San Diego, 2013.
- 688 Hester, E. T., and Gooseff, M. N.: Moving beyond the banks: Hyporheic restoration is  
689 fundamental to restoring ecological services and functions of streams,  
690 Environmental Science and Technology, 44 (5), 1521-1525, 2010.
- 691 Hunt, B.: An approximation for the bank storage effect, Water Resources Research, 26  
692 (11), 2769–2775, 1990.
- 693 Kiel, B. A., Cardenas, M. B.: Lateral hyporheic exchange throughout the Mississippi  
694 River network, Nature Geoscience, 7 (6), 413-417, 2014.
- 695 Krause, S., Abbott, B. W., Baranov, V., Bernal, S., Blaen, P., Datry, T., Drummond, J.,  
696 Fleckenstein, J. H., Gomez-Velez, J., Hannah, D. M., Knapp, J. L. A., Kurz, M.,  
697 Lewandowski, J., Marti, E., Mendoza-Lera C., Milner, A., Packman, A., Pinay,  
698 G., Ward, A. S., Zarnetzke, J. P.: Organizational principles of hyporheic  
699 exchange flow and biogeochemical cycling in river networks across scales,  
700 Water Resources Research. 58, e2021WR029771, 2022.



- 
- 701 Krause, S., Hannah, D. M., Fleckenstein, J. H., Heppell, C. M., Pickup, R., Pinay, G.,  
702 Robertson, A. L., and Wood, P. J.: Inter-disciplinary perspectives on processes in  
703 the hyporheic zone, *Ecohydrology Journal*. 4 (4), 481-499, 2011.
- 704 Krause, S., Lewandowski, J., Grimm, N., Hannah, D. M., Pinay, G., Turk, V., Argerich,  
705 A., Sabater, F., Fleckenstein, J., Schmidt, C., Battin, T., Pfister, L., Martí, E.,  
706 Sorolla, A., Lamed, S., and Turk, V.: Ecohydrological interfaces as critical  
707 hotspots for ecosystem functioning, *Water Resources Research*. 53, 6359-6376,  
708 2017.
- 709 Krause, S., Tecklenburg, C., Munz, M., and Naden, E.: Streambed nitrogen cycling  
710 beyond the hyporheic zone: Flow controls on horizontal patterns and depth  
711 distribution of nitrate and dissolved oxygen in the upwelling groundwater of a  
712 lowland river, *Journal of Geophysical Research: Biogeosciences*, 118 (1), 54-67,  
713 2013.
- 714 Kruegler, J., Gomez-Velez, J. D., Lautz, L. K., and Endreny, T. A.: Dynamic  
715 evapotranspiration alters hyporheic flow and residence times in the intrameander  
716 zone, *Water*, 12 (2), 424, 2020.
- 717 Larkin, R. G., and Sharp, J. M.: On the relationship between river-basin  
718 geomorphology, aquifer hydraulics, and groundwater flow direction in alluvial  
719 aquifers, *Geological Society of America Bulletin*, 104, 1608-1620, 1992.
- 720 Li, H., Boufadel, M. C., and Weaver, J. W.: Quantifying bank storage of variably  
721 saturated aquifers, *Ground Water*, 46 (6), 841-850, 2008.
- 722 Liang, X. Y., Zhan, H. B., and Schilling, K.: Spatiotemporal responses of groundwater  
723 flow and aquifer-river exchanges to flood events, *Water Resources Research*, 54  
724 (3), 1513-1532, 2018.
- 725 Lindow, N., Fox, G. A., and Evans, R. O.: Seepage erosion in layered stream bank  
726 material, *Earth Surface Processes and Landforms*, 34 (12), 1693-1701, 2009.
- 727 Mayor, Á. G., Bautista, S., Small, E. E., Dixon, M., and Bellot, J.: Measurement of  
728 the connectivity of runoff source areas as determined by vegetation pattern and





- 
- 729 topography: A tool for assessing potential water and soil losses in drylands,  
730 Water Resources Research, 44 (10), 2008.
- 731 Maury, B.: Characteristics ALE method for the unsteady 3D Navier-Stokes equations  
732 with a free surface, International Journal of Computational Fluid Dynamics, 6 (3),  
733 175-188, 1996.
- 734 McCallum, J.L., P.G. Cook, P. Brunner, and D. Berhane.: Solute dynamics during  
735 bank storage flows and implications for chemical baseflow separation, Water  
736 Resources Research, 46: W07541, 2010.
- 737 McClain, M. E., Boyer, E. W., Dent, C. L., Gergel, S. E., Grimm, N. B., Groffman, P.  
738 M., Hart, S. C., Harvey, J. W., Johnston, C. A., Mayorga, E., McDowell, W and  
739 Pinay, G.: Biogeochemical hot spots and hot moments at the interface of  
740 terrestrial and aquatic ecosystems, Ecosystems, 6 (4), 301-312, 2003.
- 741 Millar, R. G., and Quick, M. C.: Effect of bank stability on geometry of gravel rivers,  
742 Journal of Hydraulic Engineering, 119 (12), 1343-1363, 1993.
- 743 Millington, R. J., and Quirk, J. P.: Permeability of porous solids, Transactions of the  
744 Faraday Society, 57, 1200-1207, 1961.
- 745 Osman, A. M., and Thorne, C. R.: Riverbank stability analysis. I: Theory, Journal of  
746 Hydraulic Engineering, 114 (2), 134-150, 1988.
- 747 Pinay, G., Peiffer, S., De Dreuzy, J. R., Krause, S., Hannah, D. M., Fleckenstein, J. H.,  
748 Sebilo, M., Bishop, K., and Hubert-M, L.: Upscaling nitrogen removal capacity  
749 from local hotspots to low stream orders' drainage basins, Ecosystems, 18 (6),  
750 1101-1120, 2015.
- 751 Pohjoranta, A., and Tenno, R.: Implementing surfactant mass balance in 2D  
752 FEM-ALE models, Engineering with Computers, 27 (2), 165-175, 2011.
- 753 Puttock, A., Macleod, C. J., Bol, R., Sessford, P., Dungait, J., and Brazier, R. E.:  
754 Changes in ecosystem structure, function and hydrological connectivity control  
755 water, soil and carbon losses in semi-arid grass to woody vegetation transitions,  
756 Earth Surface Processes and Landforms, 38 (13), 1602-1611, 2013.



- 
- 757 Seminara, G.: Meanders, *Journal of Fluid Mechanics*, 554, 271-297, 2006.
- 758 Schmadel, N. M., A. S. Ward, C. S. Lowry, and J. M. Malzone.: Hyporheic exchange  
759 controlled by dynamic hydrologic boundary conditions, *Geophysical Research*  
760 *Letters*, 43, 4408-4417, 2016.
- 761 Sharp, J. M.: Limitations of bank-stopage model assumptions, *Journal of Hydrology*,  
762 35 (1-2), 31-47, 1977.
- 763 Siergieiev, D., Ehlert, L., Reimann, T., Lundberg, A., and Liedl, R.: Modelling  
764 hyporheic processes for regulated rivers under transient hydrological and  
765 hydrogeological conditions, *Hydrology and Earth System Sciences*, 19 (1),  
766 329-340, 2015.
- 767 Singh, T., Gomez-Velez, J. D., Wu, L., Wörman, A., Hannah, D. M., and Krause, S.:  
768 Effects of successive peak flow events on hyporheic exchange and residence  
769 times, *Water Resources Research*, 56 (8), e2020WR027113, 2020.
- 770 Singh, T., Wu, L., Gomez-Velez, J. D., Lewandowski, J., Hannah, D. M., Krause, S.:  
771 Dynamic hyporheic zones: Exploring the role of peak flow events on bedform-  
772 induced hyporheic exchange, *Water Resources Research*, 55, 218-235, 2019.
- 773 Stonedahl, S. H., Harvey, J. W., and Packman, A. I.: Interactions between hyporheic  
774 flow produced by stream meanders, bars, and dunes, *Water Resources Research*,  
775 49, 5450-5461, 2013.
- 776 Triska, F. J., Kennedy, V. C., Avanzino, R. J., Zellweger, G. W., and Bencala, K. E.:  
777 Retention and transport of nutrients in a third - order stream in northwestern  
778 California: Hyporheic processes, *Ecology*, 70 (6), 1893-1905, 1989.
- 779 Weatherill, J. J., Atashgahi, S., Schneidewind, U., Krause, S., Ullah, S., Cassidy, N.,  
780 and Rivett, M. O.: Natural attenuation of chlorinated ethenes in hyporheic zones:  
781 A review of key biogeochemical processes and in-situ transformation potential,  
782 *Water research*, 128, 362-382, 2018.
- 783 Wondzell, S. M., and Swanson, F. J.: Floods, channel change, and the hyporheic zone,  
784 *Water Resources Research*, 35 (2), 555-567, 1999.



- 
- 785 Wu, L., Gomez-Velez, J. D., Krause, S., Singh, T., Wörman, A., and Lewandowski, J.:  
786 Impact of flow alteration and temperature variability on hyporheic exchange,  
787 Water Resources Research, 56 (3), e2019WR026225, 2020.
- 788 Wu, L., Gomez-Velez, J. D., Krause, S., Wörman, A., Singh, T., Nützmann, G., and  
789 Lewandowski, J.: How daily groundwater table drawdown affects the diel  
790 rhythm of hyporheic exchange, Hydrology and Earth System Sciences, 25 (4),  
791 1905-1921, 2021.
- 792 Wu, L., Singh, T., Gomez-Velez, J. D., Nützmann, G., Wörman, A., Krause, S., and  
793 Lewandowski, J.: Impact of dynamically changing discharge on hyporheic  
794 exchange processes under gaining and losing groundwater conditions, Water  
795 Resources Research, 54 (12), 10-076, 2018.
- 796 Zarnetske, J. P., Haggerty, R., Wondzell, S. M., and Baker, M. A.: Dynamics of nitrate  
797 production and removal as a function of residence time in the hyporheic zone,  
798 Journal of Geophysical Research, 116, G01025, 2021.
- 799 Zarnetske, J. P., Haggerty, R., Wondzell, S. M., Bokil, V. A., and González-Pinzón, R.:  
800 Coupled transport and reaction kinetics control the nitrate source-sink function of  
801 hyporheic zones, Water Resources Research, 48, W11508, 2012.
- 802 Zingg, A. W.: Degree and length of land slope as it affects soil loss in run-off,  
803 Agricultural Engineering, 21, 59-64, 1940.
- 804